

Bayesian implications of current LHC supersymmetry and dark matter detection searches for the Constrained MSSM

Leszek Roszkowski*, Enrico Maria Sessolo and Yue-Lin Sming Tsai

National Centre for Nuclear Research, Hoża 69, 00-681 Warsaw, Poland

Abstract

We investigate the impact of recent limits from LHC searches for supersymmetry and from direct and indirect searches for dark matter on global Bayesian inferences of the parameter space of the Constrained Minimal Supersymmetric Standard Model (CMSSM). In particular we apply recent exclusion limits from the CMS α_T analysis of 1.1 fb^{-1} of integrated luminosity, the current direct detection dark matter limit from XENON100, as well as recent experimental constraints on γ -ray fluxes from dwarf spheroidal satellite galaxies of the Milky Way from the FermiLAT telescope, in addition to updating values for other non-LHC experimental constraints. We extend the range of scanned parameters to include a significant fraction of the focus point/hyperbolic branch region. While we confirm earlier conclusions that at present LHC limits provide the strongest constraints on the model's parameters, we also find that when the uncertainties are not treated in an excessively conservative way, the new bounds from dwarf spheroidals have the power to significantly constrain the focus point/hyperbolic branch region. Their effect is then comparable, if not stronger, to that from XENON100. We further analyze the effects of one-year projected sensitivities on a neutrino flux from the Sun in the 86-string IceCube+DeepCore configuration at the South Pole. We show that data on neutrinos from the Sun, expected for the next few months at IceCube and DeepCore, have the potential to further constrain the same region of parameter space independently of the LHC and can yield additional investigating power for the model.

*On leave of absence from the University of Sheffield.

1 Introduction

The Large Hadron Collider (LHC) at CERN started its run at center of mass energy $\sqrt{s} = 7$ TeV more than a year ago, and in 2011 published several results based on an integrated luminosity of 1.1 fb^{-1} [1, 2]. Several searches were performed, aimed at the discovery of signatures that might be an indication of new physics beyond the Standard Model (SM). One of the scenarios that is most appealing and well motivated from a theoretical point of view is softly broken supersymmetry (SUSY) (see, e.g., Ref. [3]). In the past 25 years or so there has been vast proliferation of models for SUSY-breaking. Among models that are mediated by gravitational interactions, the Constrained Minimal Supersymmetric Standard Model (CMSSM) [4] is the most popular because of reasonable unification assumptions and a reduced number of parameters. In the CMSSM, three parameters are defined at the scale of grand unification: the universal scalar mass m_0 , the universal gaugino mass $m_{1/2}$, and the universal trilinear coupling A_0 . Additionally, $\tan\beta$ (the ratio of the expectation values of the two Higgs doublets) is defined at the electroweak scale, while the sign of the Higgs/higgsino parameter μ remains undetermined.

Recently, there have been many studies, both experimental and phenomenological, of the impact of bounds from new physics searches at the LHC on the parameter space (PS) of the CMSSM [5, 6, 7, 8]. In particular, a recent α_T analysis [1] excluded for most MSSM models observation of the lightest squarks with mass $m_{\tilde{q}} \lesssim 700$ GeV, and gluinos with $m_{\tilde{g}} \lesssim 580$ GeV at the 95% confidence level (C.L.). Under sensible assumptions, these limits translate into an exclusion bound in the $(m_0, m_{1/2})$ plane at fixed $A_0 = 0$, $\tan\beta = 10$. The bound is shown in Fig. 8 of Ref. [1].

Recently, an updated Bayesian analysis of the CMSSM, which included the α_T bound from CMS, was performed by some of the authors of this paper [9]. The analyzed region covered the range $m_0 \leq 2$ TeV, $m_{1/2} \leq 1$ TeV, and also included the improved limits on the spin-independent (SI) neutralino-proton cross section σ_p^{SI} from direct detection (DD) of dark matter (DM) with 100.9 days of live data at XENON100 [10, 11, 12]. One of the main findings of [9] was that LHC limits currently have the most constraining effect on the PS of the CMSSM, while a further impact of the DD limit from XENON100 is limited after theoretical and astrophysical uncertainties are taken into account.

The study [9] also showed that a combination of the new LHC limits with the previously considered usual non-LHC constraints, particularly from flavor physics [$b \rightarrow s\gamma$, $(g-2)_\mu$, $B_s \rightarrow \mu^+\mu^-$, etc.], dark matter abundance $\Omega_\chi h^2$, and LEP, results in two broad regions of high posterior probability. One is located at large $m_{1/2}$ and small m_0 and agrees reasonably well with the findings of studies using a frequentist approach [6]. In addition, a sizable region remains in the focus point/hyperbolic branch (FP/HB) region [3, 13], the part of PS at large m_0 , and $m_{1/2} < m_0$.

In this paper we look deeper into the FP/HB region and perform a Bayesian analysis of the

CMSSM with its soft mass parameters extended to $m_0 \leq 4$ TeV and $m_{1/2} \leq 2$ TeV, which is for each parameter twice as large as in [9]. While generally inaccessible to direct LHC searches for SUSY, the FP/HB region can be probed by results from DD of DM, and further constraints can be derived from recent results on indirect detection (ID). In that respect, in addition to updated constraints used in [9], we apply the recent upper bounds on the annihilation cross section of neutralinos obtained by the FermiLAT Collaboration [14] from γ -ray fluxes from dwarf spheroidal satellite galaxies of the Milky Way (dSphs). Additionally, we discuss the impact of the one-year 95% C.L. sensitivities for observation of high energy neutrinos from the Sun at IceCube and DeepCore [15].

A full list of constraints applied here and also in [9] will be given below. Recently, the impact on the CMSSM parameters of LHC limits and DD (but not ID) limits on DM was also investigated in Refs. [6, 7, 8]. Reference [6] adopted frequentist statistics and [7] performed a fixed-grid scan in contrast to our Bayesian one, while Refs. [8] included a different set of constraints. In contrast, the main goal of this paper is to analyze the impact of ID searches.

In Sec. 2 we summarize the main features of Bayesian inference and describe our scanning methodology. We explain our implementation of the LHC and XENON100 constraints in Sec. 3. In Sec. 4 we describe our implementation of the bounds from dSphs into the CMSSM PS, and detail our calculation of the IceCube/DeepCore sensitivities. We discuss our results in Sec. 5, and finally give our summary and conclusions in Sec. 6.

2 Methodology

In Bayesian statistics, for a theory described by some parameters m , experimental observables $\xi(m)$ can be compared with data d and a posterior probability density function (pdf) $p(m|d)$ can be calculated through Bayes' Theorem

$$p(m|d) = \frac{p(d|\xi(m))\pi(m)}{p(d)}, \quad (1)$$

where the likelihood $p(d|\xi(m))$ gives the probability density for obtaining d from a measurement of ξ , the prior $\pi(m)$ parametrizes assumptions about the theory prior to performing the measurement, and the evidence $p(d)$ represents the assumptions on the data. As long as one considers only one model (as we do in this paper) it is a constant in theory parameters and thus a normalization factor. The Bayesian approach yields a simple and natural procedure for calculating the posterior pdf of any limited subset of r variables in PS, $\psi_{i=1,\dots,r} \subset m$. One just needs to marginalize, or integrate, over the remaining parameters

$$p(\psi_{i=1,\dots,r}|d) = \int p(m|d) d^{n-r} m, \quad (2)$$

where n denotes the dimension of the full PS. To describe our methodology for the Bayesian scan, we use the same notation as [9].

We scan over the CMSSM parameters $(m_0, m_{1/2}, A_0, \tan \beta)$, which are incorporated in the likelihood function according to the procedure detailed in [16]. The Bayesian approach also allows a consistent treatment of residual uncertainties in the SM. In the CMSSM, the relevant “nuisance” parameters are [16] the pole mass of the top quark m_t^{pole} , the mass of the bottom quark at its nominal scale in the \overline{MS} scheme, $m_b(m_b)^{\overline{MS}}$, and the strong and inverse electromagnetic coupling constants at the Z pole in the \overline{MS} scheme, $\alpha_s(M_Z)^{\overline{MS}}$ and $1/\alpha_{em}(M_Z)^{\overline{MS}}$, respectively.

We perform our scan in the following ranges:

$$\begin{aligned}
100 \text{ GeV} &\leq m_0 \leq 4000 \text{ GeV} \\
100 \text{ GeV} &\leq m_{1/2} \leq 2000 \text{ GeV} \\
-2000 \text{ GeV} &\leq A_0 \leq 2000 \text{ GeV} \\
3 &\leq \tan \beta \leq 62.
\end{aligned}
\tag{3}$$

$\text{sgn} \mu$ is fixed at +1 to accommodate the discrepancy of $(g-2)_\mu$ with SM predictions [17]. The nuisance parameters are scanned in the ranges

$$\begin{aligned}
163.7 \text{ GeV} &\leq m_t^{\text{pole}} \leq 178.8 \text{ GeV} \\
3.92 \text{ GeV} &\leq m_b(m_b)^{\overline{MS}} \leq 4.48 \text{ GeV} \\
0.1096 &\leq \alpha_s(M_Z)^{\overline{MS}} \leq 0.1256 \\
127.846 &\leq 1/\alpha_{em}(M_Z)^{\overline{MS}} \leq 127.99.
\end{aligned}
\tag{4}$$

We adopt logarithmic priors in m_0 and $m_{1/2}$ throughout our analysis, and we refer the reader to the relevant literature [16, 17] for a discussion on the incidence of linear priors on SUSY PS scans. The observables we use to constrain the PS, and their experimental and theoretical errors, are reported in Table 1 and are the same as given in Ref. [9]. We perform our global scan with the package SuperBayeS [18], which we have modified to our needs. As stated above, the non-LHC constraints have been updated with respect to previous papers. To these we add the LHC, DD, and ID constraints, which we describe in some detail below.

3 LHC and DD constraints

3.1 The α_T SUSY search

In order to calculate the likelihood for the LHC signal, we generally follow the procedure detailed in Ref. [9]. With respect to the previous paper, we extend the efficiency maps to the larger values

Observable	Mean	Exp. Error	Theor. Error	Likelihood Distribution	Reference
Non-LHC:					
$\Omega_\chi h^2$	0.1120	0.0056	10%	Gaussian	[19]
$\sin^2 \theta_{\text{eff}}$	0.231160	0.00013	15.0×10^{-5}	Gaussian	[20]
M_W	80.399	0.023	0.015	Gaussian	[20]
$\delta(g-2)_\mu^{SU5Y} \times 10^{10}$	30.5	8.6	1	Gaussian	[20, 21]
$\mathcal{BR}(\bar{B} \rightarrow X_s \gamma) \times 10^4$	3.6	0.23	0.21	Gaussian	[20]
$\mathcal{BR}(B_u \rightarrow \tau \nu) \times 10^4$	1.66	0.66	0.38	Gaussian	[22]
ΔM_{B_s}	17.77	0.12	2.4	Gaussian	[20]
$\mathcal{BR}(B_s \rightarrow \mu^+ \mu^-)$	$< 1.5 \times 10^{-8}$	0	14%	Upper limit — Error fn	[23]
LEP — 95% Limits					
m_h	> 114.4	0	3	Lower limit — Error fn	[24]
ζ_h^2	$< f(m_h)$	0	0	Upper limit — Step fn	[24]
m_χ	> 50	0	5%	Lower limit — Error fn [25] ([26, 27])	
$m_{\chi_1^\pm}$	> 103.5 (92.4)	0	5%	Lower limit — Error fn [28] ([26, 27])	
$m_{\tilde{e}_R}$	> 100 (73)	0	5%	Lower limit — Error fn [28] ([26, 27])	
$m_{\tilde{\mu}_R}$	> 95 (73)	0	5%	Lower limit — Error fn [28] ([26, 27])	
$m_{\tilde{\tau}_1}$	> 87 (73)	0	5%	Lower limit — Error fn [28] ([26, 27])	
$m_{\tilde{\nu}}$	> 94 (43)	0	5%	Lower limit — Error fn [29] ([20])	
LHC CMS α_T 1.1/fb analysis					
α_T	See text	See text	0	Poisson	[1]
XENON100					
$\sigma_p^{\text{SI}}(m_\chi)$	$< f(m_\chi)$ — see text	0	1000%	Upper limit — Error fn	[12]
Nuisance					
$1/\alpha_{em}(M_Z)^{\overline{MS}}$	127.916	0.015	0	Gaussian	[20]
m_t^{pole}	172.9	1.1	0	Gaussian	[20]
$m_b(m_b)^{\overline{MS}}$	4.19	0.12	0	Gaussian	[20]
$\alpha_s(M_Z)^{\overline{MS}}$	0.1184	0.0006	0	Gaussian	[20]

Table 1: The experimental measurements that constrain the CMSSM’s parameters and the Standard Model’s nuisance parameters. Masses are in GeV. The numbers in parentheses in the list of LEP experimental measurements are weaker experimental bounds, which we use for some sparticle mass hierarchies.

of m_0 and $m_{1/2}$ considered here, and improve the evaluation of the detector efficiency. While in [9] the geometrical acceptance was applied to simulate the CMS detector response, here we apply the kinematical cuts detailed in the experimental paper [1] with the fast detector simulator PGS4 [30], whose parameters have been set to the specifications given by the CMS Collaboration. Besides, we slightly improve the minimization procedure for the difference in missing transverse energy of the pseudojets. We have compared our efficiency maps for $A_0 = 0$ and $\tan\beta = 10$ with the results of [9] in the overlapping region, finding excellent agreement.

3.2 XENON100 bound

We incorporate in our scan the constraints induced on the SI neutralino-proton cross section σ_p^{SI} by the 90% C.L. upper bound $\sigma_{p,90}^{\text{SI}}$, which was recently published by the XENON100 Collaboration [10, 11, 12]. As described in the experimental papers, the bound is obtained from the p -value of a likelihood function which includes the systematic and statistical error in signal and background, as well as the uncertainties on scintillation efficiency and escape velocity; see [11] for details. However, the experimental analysis does not consider the astrophysical uncertainties associated with the chosen velocity distribution and DM halo profile [31, 32, 33], nor the nuclear physics uncertainties associated with calculations of the π -nucleon sigma term $\Sigma_{\pi N}$ [34], which are in fact dominant. Here and below we denote these theoretical uncertainties with τ . (In contrast, we label the experimental uncertainties with σ .) The uncertainties τ have been quantified in the literature and amount up to approximately 10 times the upper bound on the cross section, $\tau \sim 10 \times \sigma_{p,90}^{\text{SI}}$ [9]. We include τ in the likelihood, following the procedure described in [16] for the treatment of upper bounds. This procedure allows for a systematic treatment of the mismatch between true ($\hat{\xi}$) and approximate (ξ) theoretical quantities; see [16] for details. In the limit of negligible σ , the likelihood function is given by a convolution of a step function, $\lim_{\sigma \rightarrow 0} p(\sigma, \sigma_{p,90}^{\text{SI}} | \hat{\xi}) \equiv \Theta(\sigma_{p,90}^{\text{SI}} - \hat{\xi})$, and a Gaussian function parametrizing the theoretical uncertainties, $p(\hat{\xi} | \xi, \tau) \equiv \text{Gauss}(\xi, \tau)$, where in this case $\xi = \sigma_p^{\text{SI}}$. The result is a complementary error function likelihood which smears out the experimental bound at the desired level,

$$p(\sigma_{p,90}^{\text{SI}} | \xi, \tau) = \frac{1}{2} \text{erfc} \left(\frac{\xi - \sigma_{p,90}^{\text{SI}}}{\sqrt{2}\tau} \right), \quad (5)$$

where the error function $\text{erfc}(x)$ is defined in the standard way,

$$\text{erfc}(x) \equiv \frac{2}{\sqrt{\pi}} \int_x^\infty e^{-t^2} dt. \quad (6)$$

Since it is obvious (and has been shown in [9]) that such a large theoretical uncertainty greatly reduces the impact of the XENON100 upper bound, for comparison we consider here the idealized case where τ is much reduced and is assumed to be comparable in size to $\sigma_{p,90}^{\text{SI}}$. We do this to quantify the “bare” effect of the experimental bound on our PS.

Two recent papers [8] also considered the impact of the XENON100 bound on CMSSM PS in the Bayesian framework but their treatment of the theoretical uncertainties differs from ours. Unlike us, they do not smear out the experimental bound, but instead include the theoretical uncertainties in the scan as nuisance parameters and eventually marginalize over them. While in principle this is an appropriate procedure in the context of Bayesian statistics, when uncertainties arise from having a number of calculations which are based on different assumptions and methodologies and thus yield incompatible results, as is the case with the spread in the $\Sigma_{\pi N}$ uncertainty [34], it is difficult to believe that they follow any statistical distribution.

More importantly, as we will see below, even by choosing an extremely optimistic (and, for the foreseeable future, rather unrealistically) small value of τ , say $\tau = \sigma_{p,90}^{\text{SI}}$, the XENON100 bound affects the PS only weakly. This is because current LHC limits have a much stronger impact on the CMSSM parameters [9]. As we will show below, unless one neglects the theoretical uncertainties altogether, thus taking the experimental bound at face value as a hard cut, the impact of the bound $\sigma_{p,90}^{\text{SI}}$ on the FP region remains limited.

4 ID constraints

Besides direct searches at accelerators and underground DM detectors, the third direction in the quest for DM discovery is to use detectors to look for uncharacteristic signatures pointing to physics beyond the SM in cosmic ray radiation. One method for ID of DM is to exploit searches for γ -ray spectra characteristic of DM annihilation [14, 35, 36, 37]. Another one is the search for high energy neutrinos from annihilation of weakly interactive massive particles (WIMPs) in the Sun or (to minor extent) Earth in neutrino telescopes like IceCube [15].

4.1 The FermiLAT γ -ray telescope

We will focus in this subsection on γ rays, leaving neutrinos to the next. The FermiLAT detector [35] in the Fermi satellite has been used in the past few years on several targets for detection of γ rays from DM annihilation. Both multiwavelength and line searches have been performed [36]. Recently, data were published by the FermiLAT Collaboration which improved significantly the previous sensitivities to DM searches. The most luminous source is the Galactic center (GC) in the Milky Way, but it is also subject to a higher astrophysical background. Better upper limits on the DM annihilation cross section were obtained from the γ -ray fluxes of a few dwarf spheroidal satellite galaxies (dSphs) [38, 37, 14] of the Milky Way. They are less luminous but completely dominated by DM, with little presence of gases or stars.

The differential flux of DM annihilation-induced γ rays from a generic target satellite galaxy is

given by

$$\Phi(E) = \frac{N_\gamma(E)}{8\pi} \frac{\langle\sigma v\rangle_{\text{ann}}}{m_\chi^2} \int_{\Delta\Omega} \int_{l_-}^{l_+} \rho^2[l(\theta)] dl(\theta) d\Omega, \quad (7)$$

where $N_\gamma(E)$ is the photon energy distribution per annihilation, $\langle\sigma v\rangle_{\text{ann}}$ is the velocity-averaged pair-annihilation cross section, and m_χ is the WIMP mass. l is the line-of-sight distance, which depends on the opening angle θ from the center of the galaxy; the integration limits read $l_\pm = D \cos \theta \pm \sqrt{r_t^2 - D^2 \sin^2 \theta}$, where D is the distance to the target galaxy, and r_t is the tidal radius of the DM halo. $\rho(l)$ is the DM density distribution in the galaxy, and the angular integration is performed about a solid angle $\Delta\Omega$ calculated by pointing the z axis of the reference frame in the direction of the galaxy. The double integral in Eq. (7) is commonly referred to as the J -factor, whose determination depends on the selected DM galactic profile, and on uncertainties in the stellar velocity distribution in the galaxy. In a recent publication [14], the FermiLAT Collaboration improved their previous analysis on dSphs [37] by (a) including two more dSphs in their original set of eight and (b) incorporating the velocity uncertainties on the J -factor in a likelihood approach. The DM density distribution was assumed to follow a cuspy Navarro-Frenk-White (NFW) profile [39], and its normalization and scale factor were obtained by comparisons with stellar velocity observations through the likelihood approach. By applying this technique, the collaboration derived a stronger 95% C.L. upper bounds on the annihilation cross sections, $\langle\sigma v\rangle_{i,95}$ as a function of m_χ , for different final-state channels ($i = b\bar{b}, \mu^-\mu^+, \tau^-\tau^+, W^-W^+$). The bounds are reported in Fig. 2 of Ref. [14].

In this paper we investigate the effects of the limits $\langle\sigma v\rangle_{i,95}$ on the CMSSM PS. In order to effectively constrain our Bayesian credible regions, we need to be able to invert the procedure that the experimental group used to translate an upper limit on the DM-related photon flux into a bound on a cross section. The 95% C.L. upper bound on the photon flux as a function of energy $\Phi_{95}(E)$ was not reported in [14]. The collaboration obtained it through the energy-binned likelihood function given in their Eq. (1). The bound depends nontrivially on the flux actually observed by the detector, the known background, and the astrophysical uncertainties.

We can approximately reconstruct Φ_{95} from any of the given limits $\langle\sigma v\rangle_{i,95}$ through Eq. (7), since each limit was obtained under the single-final-state assumption. To illustrate the procedure, let us select one final-state channel, say $b\bar{b}$. The photon spectrum from $b\bar{b}$ cascades, $N_\gamma^{(b\bar{b})}(E)$, does not depend on the nature of the DM particle. Thus, we can eliminate the energy dependence by integrating over the FermiLAT spectral sensitivity range, from 0.2 GeV to 100 GeV: $N_{b\bar{b}} \equiv \int N_\gamma^{(b\bar{b})}(E) dE$. Assuming the branching ratio $\text{BR}_{b\bar{b}} = 1$, the upper bound on the annihilation cross section as a function of m_χ is related to the upper bound on the photon flux through Eq. (7): $\langle\sigma v\rangle_{b\bar{b},95} = 8\pi m_\chi^2 \bar{\Phi}_{95} / (N_{b\bar{b}} J)$, where J denotes the J -factor and $\bar{\Phi}_{95} \equiv \int \Phi_{95}(E) dE$.

In the MSSM neutralino pair annihilation proceeds through several final states, both at the tree

and loop level. From the above discussion it is easy to see that the 95% C.L. bound on the total annihilation cross section $\langle\sigma v\rangle_{\text{ann},95}$ of the MSSM can be obtained from the equality,

$$\bar{\Phi}_{95} = \frac{N_{b\bar{b}}\langle\sigma v\rangle_{b\bar{b},95} J}{8\pi m_\chi^2} = \frac{(\sum_{i=1}^{29} \text{BR}_i N_i)\langle\sigma v\rangle_{\text{ann},95} J}{8\pi m_\chi^2}, \quad (8)$$

from which one obtains

$$\langle\sigma v\rangle_{\text{ann},95} = \frac{\langle\sigma v\rangle_{b\bar{b},95} \cdot N_{b\bar{b}}}{\sum_{i=1}^{29} \text{BR}_i N_i}, \quad (9)$$

where we sum the branching ratios $\text{BR}_i \equiv \langle\sigma v\rangle_i/\langle\sigma v\rangle_{\text{ann}}$ over all 29 channels implemented in SuperBayeS. In order to reduce the uncertainties, we performed this procedure three times, using the $\langle\sigma v\rangle_{b\bar{b},95}$, $\langle\sigma v\rangle_{\mu^-\mu^+,95}$, and $\langle\sigma v\rangle_{\tau^-\tau^+,95}$ lines. The resulting likelihoods were eventually multiplied together. We neglected the WW line because the channel opens up only at $m_\chi \sim m_W$, giving less constraining power on our PS than the other channels.

It has been long known from studies of the impact of γ -ray fluxes from the GC (see e.g. [40]) that the uncertainties in the halo profile play a significant role in the determination of the derived cross section bounds. As Eq. (7) shows, the assumptions on the DM halo profile affect the J -factor, sometimes by orders of magnitude, thus introducing an uncertainty in the photon flux received at the detector. On the other hand, a recent study on dSphs' DM density profiles [41] showed that the analysis of stellar velocity dispersions of some dSph candidates imposes strong constraints on the mass within the half-light radius. When these constraints are taken into account, calculating the J -factor under the assumption of a NFW-like DM density profile yields photon fluxes which are comparable or somewhat lower than those obtained with smoother, corelike profiles. The cross sections given in [14] are therefore conservative, and the 1σ uncertainties resulting from the likelihood procedure amount to approximately 3%. In light of this, in our scan we considered the theoretical uncertainty to be zero and smeared the 95% C.L. bound by a half Gaussian with uncertainty 3%. This is the Bayesian equivalent to performing a hard cut on the PS and results from taking the limit $\tau \rightarrow 0$ in Eq. (3.5) of Ref. [16].

4.2 Neutrino telescopes

In 2010 the construction of all 86 strings of the IceCube neutrino telescope at the South Pole was eventually completed [42]. The instrumented volume covers approximately 1 km^3 and deploys 80 strings uniformly spaced 125 m from one another, which carry 60 optical modules each. The energy threshold of the muon effective area is estimated by the experimental collaboration to be approximately 100 GeV [43]. DeepCore, an additional array of six denser strings, is also operational. Its performance is parametrized by the muon effective volume V_{eff} . The energy dependence of V_{eff} is plotted in [44], and its parametrization can be found in [45]. The resulting energy threshold is $E_{\text{min}} \sim 35 \text{ GeV}$.

The IceCube Collaboration published in 2009 the first results on a search for neutrinos from neutralino annihilation in the Sun, with 104.3 live days of data taking in their 22-string configuration [46]. No excess over the atmospheric background was detected. Recently, the collaboration published a new report with the results from a combined analysis of 812 days of lifetime data from AMANDA-II in the years 2001 – 2006, as well as 149 days in 2008 – 09 for the 40-string IceCube detector [47]. The data again show no excess over the background. On the other hand, this implies a more stringent upper bound on the spin-dependent (SD) neutralino-proton cross section, and thus the data are starting to bite into regions of SUSY PS that were previously probed only by DD experiments. While presently available data do not allow us to draw any definite conclusions, the results for the full configuration (which should be published soon) will have significant constraining power, as noted already in Refs. [48, 49, 50]. Moreover, in recent years the study of the detector sensitivity has become more elaborate, including increasingly detailed detector simulations [51, 44, 45].

In this paper, we show the impact of the expected one-year 95% C.L. sensitivities for the full configuration of IceCube and DeepCore on CMSSM PS, in light of the constraints from the LHC, DD, and ID described in the previous sections. With respect to [48, 49], in addition to a more accurate treatment of the most constraining limit from LHC results, we update the effective areas and volumes to the most recent values [44, 45] and investigate the separate impacts of different detection channels at IceCube and DeepCore. We briefly explain the formalism below.

The differential neutrino flux on Earth is given by

$$\frac{dN}{dE_\nu} = \frac{\Gamma_{\text{eq}}}{4\pi R_{\text{SE}}^2} \sum_i \text{BR}_i \frac{dN_i}{dE_\nu}, \quad (10)$$

where Γ_{eq} is half of the WIMP capture rate, the BR_i are the branching ratios to the final products of neutralino pair annihilation, and R_{SE} is the Sun-Earth distance. Upon arriving on Earth, the neutrinos undergo charged-current (CC) interactions in and near the detector volume, thus producing a muon flux $d\Phi_\mu/dE_\mu$, which can be detected by the optical modules through Cherenkov radiation. In order to realistically approximate the detector response, we follow the procedure given in Appendix B of Ref. [44]. The muon events observed by the 80-string IceCube detector can either be labeled as *upward* (those that come from neutrinos undergoing CC scattering outside the 1-km³ instrumented volume) or as *contained* (those for which the interaction happens inside the detector). We denote the differential flux of upward muons detected by the optical modules with $d\Phi_\mu/dE_\mu^{\text{f}}$, where the index “f” is added to distinguish it from the muon flux at the interaction point, $d\Phi_\mu/dE_\mu$. The difference arises because of energy losses due to ionization, bremsstrahlung, pair production and photonuclear effects [52] that affect the spectrum of muons transiting in ice. The upward event rates at the detector are given by

$$N_{\text{events}}^{\text{up}} = \int_0^{m_\chi} \frac{d\Phi_\mu}{dE_\mu^{\text{f}}} A_{\text{eff}}(E_\mu^{\text{f}}) dE_\mu^{\text{f}}, \quad (11)$$

where $A_{\text{eff}}(E_\mu^f)$ is the muon effective area parametrized in Ref. [43]. We decided to neglect the angular dependence of the effective area since, for the signal, it integrates to a factor approximately equal to one. The expected signal rate has to be compared with the atmospheric background, which we adopted from Ref. [44], $N_{\text{BG}}^{\text{up}} \simeq 6.1 \text{ yr}^{-1}$.

The contained rate, by definition, does not suffer from propagation related losses and is given by

$$N_{\text{events}}^{\text{C}} = \int_{E_{\text{thr}}}^{m_\chi} \frac{d\Phi_\mu}{dE_\mu} (1 \text{ km}^2) dE_\mu, \quad (12)$$

where the threshold E_{thr} is conservatively fixed at 100 GeV. The background is $N_{\text{BG}}^{\text{C}} \simeq 15.6 \text{ yr}^{-1}$.

Notice that the upward and contained event rates and atmospheric backgrounds are calculated for the time of the year the Sun spends below the horizon, to reduce the background from down-going muons. So, the rates are calculated for six months' time, between the March and September equinoxes [44, 45]. For DeepCore, the larger instrumented volume outside the detector will be used to veto atmospheric muons from above the horizon, so the event rates are calculated over a 12-month period.

The events rate at DeepCore is given by

$$N_{\text{events}}^{\text{DC}} = \int_{E_{\text{min}}}^{m_\chi} \frac{1}{L} \frac{d\Phi_\mu}{dE_\mu} V_{\text{eff}}(E_\mu) dE_\mu, \quad (13)$$

where the typical scale of the detector is $L = 1 \text{ km}$, and $V_{\text{eff}}(E_\mu)$ is the effective volume shown in [44]. The background is $N_{\text{BG}}^{\text{DC}} \simeq 2.5 \text{ yr}^{-1}$.

We calculated the signal using a modified version of SuperBayeS, where we updated the muon effective area and effective volume to the values cited above. Notice that SuperBayeS (following DarkSusy [53]) uses tables from WimpSim [54] for the propagation of the neutrino flux through the Sun and to Earth, so that matter effects and neutrino oscillations are properly accounted for. Also, the signal is calculated without the approximation of thermodynamical equilibrium [53], so that the rates slightly depend on $\langle\sigma v\rangle_{\text{ann}}$. We fixed the local DM density to 0.3 GeV/cm^3 , and the root-mean-square of the velocity dispersion in the halo to 270 km/s. We compared our spectra and rates with the code used for the calculations performed in [44] and found very good agreement. Our 95% C.L. (or 2σ) projected sensitivities are calculated in the standard way, with $N_{\text{events}}/\sqrt{N_{\text{BG}}} = 2$.

5 Results in the CMSSM

In this section we will present our numerical results. First, to set the ground, we will display regions of the CMSSM mass parameters favored by current data from the usual non-LHC constraints, from the α_T constraint at the LHC, as well as from the XENON100 limit for which we will consider two

limiting cases of the theoretical error. Next, we will add the constraint from dwarf spheroidals. Finally, we will discuss the projected sensitivities at IceCube/DeepCore.

In all plots we denote as “non-LHC” the usual set of relevant constraints summarized in the first part of Table 1, while the α_T bound is indicated with “LHC(α_T).” The constraints from DD are labeled according to the size of the theoretical uncertainties assumed for them (see Sec. 3.2). In particular, when the scan is performed with the theoretical uncertainty $\tau = 10 \times \sigma_{p,90}^{\text{SI}}$, we label this with “X100($\tau=10$)”; and when we apply $\tau = 1 \times \sigma_{p,90}^{\text{SI}}$, we use the label “X100($\tau=1$).” For the dSphs bound, instead, the assumption of a NFW DM halo profile is justified by recent studies, as explained in Sec. 4. We label the ID set of constraints with “dSphs (NFW).”

5.1 Impact on the CMSSM parameter space

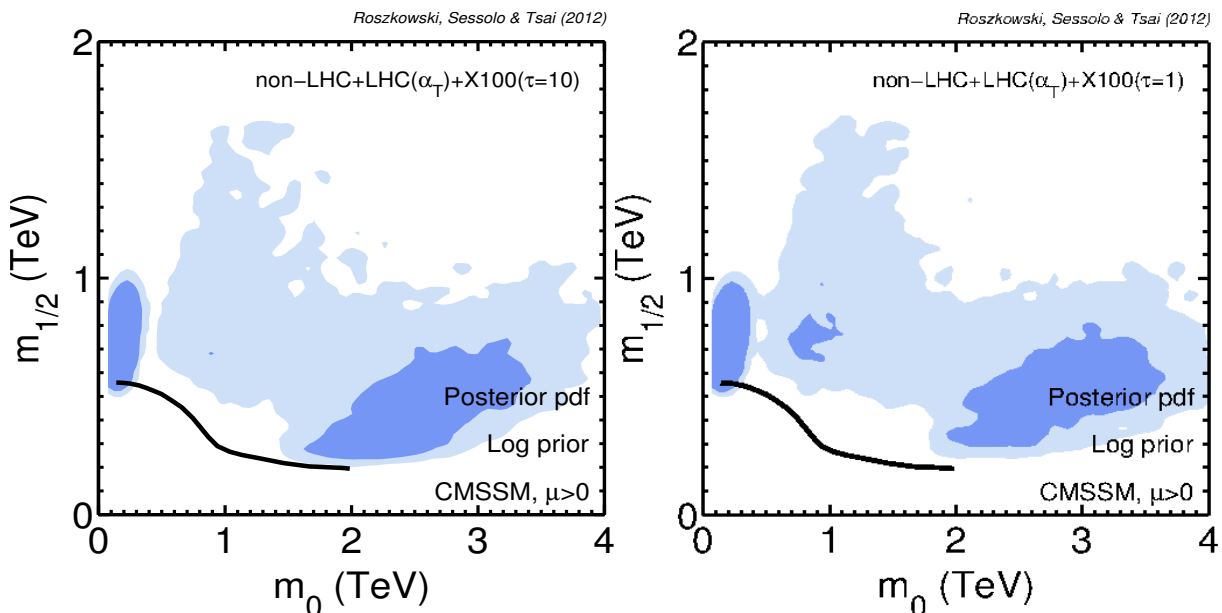


Figure 1: Marginalized posterior pdf in the $(m_0, m_{1/2})$ plane. The 68% C.L. credible regions are shown in dark blue and the 95% C.L. regions in light blue. (a) The CMSSM parameters constrained by the non-LHC, α_T , and XENON100 data. (b) The same constraints as in (a), but the theoretical uncertainty on XENON100 is strongly reduced ($\tau = 1$). The solid black line shows the 95% C.L. exclusion bound from the α_T analysis of CMS.

To start with, in Fig. 1(a) we show the marginalized posterior pdf in the $(m_0, m_{1/2})$ plane for the set of non-LHC constraints, the LHC α_T constraint from the CMS analysis of 1.1 fb^{-1} data, and the XENON100 90% C.L. bound on σ_p^{SI} with a conservative estimate of the theory error $\tau = 10 \times \sigma_{p,90}^{\text{SI}}$. Our intention here is to summarize the present impact of experimental limits on the PS of the CMSSM before we move to including the ID observations and sensitivities. We show the

68% credible posterior regions in dark blue and the 95% credible regions in light blue. The black line indicates the CMS 95% C.L. exclusion limit [1], although we stress that, as previously in [9], we apply it through our own approximate likelihood function, as discussed in Sec. 3.

The relative impact of the constraints applied in Fig. 1(a) has been extensively analyzed in [9], for a smaller range of m_0 and $m_{1/2}$. In particular, one can see the two distinct 68% posterior credible regions already found in [9]. One of these peaks in the stau-coannihilation region of the CMSSM, where m_0 is relatively small and $m_{1/2} \gtrsim 500$ GeV. (The A -resonance funnel actually extends to the much larger 2σ region.) The other appears in the FP/HB region at large m_0 and extends to much larger values of m_0 than those considered in [9]. As noted in [9], the effect of the α_T bound is mostly to push the high-probability credible regions up and outside the experimental exclusion contour.

Figure 1(a) includes the 90% C.L. bound on σ_p^{SI} with a conservative theoretical uncertainty, $\tau = 10 \times \sigma_{p,90}^{\text{SI}}$, as explained in Sec. 3.2. We have checked that removing the bound from the figure would make hardly any difference. The near independence of Fig. 1(a) on the XENON100 limit reflects the fact that at present the LHC limits are much stronger, while DD experiments are still marred by large theoretical uncertainties. We thus confirm and extend to larger parts of the FP/HB region the finding of Ref. [9] that the further effect of the current XENON100 bound on the posterior is minimal.

In Fig. 1(b) we investigate the effect of assuming a highly optimistic uncertainty of $\tau = 1 \times \sigma_{p,90}^{\text{SI}}$, as described in Sec. 3.2. One can see in Fig. 1(b) that it affects the FP/HB region by reducing the area of the 95% credible region above $m_{1/2} \sim 200$ GeV at large m_0 . The reason for this is clear: in the FP/HB region, the higgsino component of the neutralino increases, and the SI cross section with nuclei is enhanced; it thus becomes more constrained by DD limits. As a consequence of this stronger constraint on the FP/HB region, some probability is shifted towards the A -resonance funnel region, thus creating a 68% credibility “island” at $m_0 \sim 1$ TeV, which now becomes favored by the constraints from b physics and $(g-2)_\mu$. On the other hand, it appears that even by reducing the theoretical uncertainties on DD to only 100% of the experimental upper bound (a highly unlikely possibility) the impact on the PS is still not sizeable. Below we will perform a similar analysis in the $(m_\chi, \sigma_p^{\text{SI}})$ plane.

Next, in Figs. 2(a)–(b) we show the effects of the dSphs bound on γ rays from the FermiLAT Collaboration on the marginalized posterior pdf in the $(m_0, m_{1/2})$ plane and the $(A_0, \tan\beta)$ plane, respectively. Figure 2(a) shows that the bound from dSphs cuts significantly into the FP/HB region, and the impact is stronger than observed with XENON100 alone, even for the idealized case of extremely low theoretical uncertainties on σ_p^{SI} , depicted in Fig. 1(b). One can see that the bound from dSphs γ -ray fluxes significantly lowers the statistical relevance of the FP region at

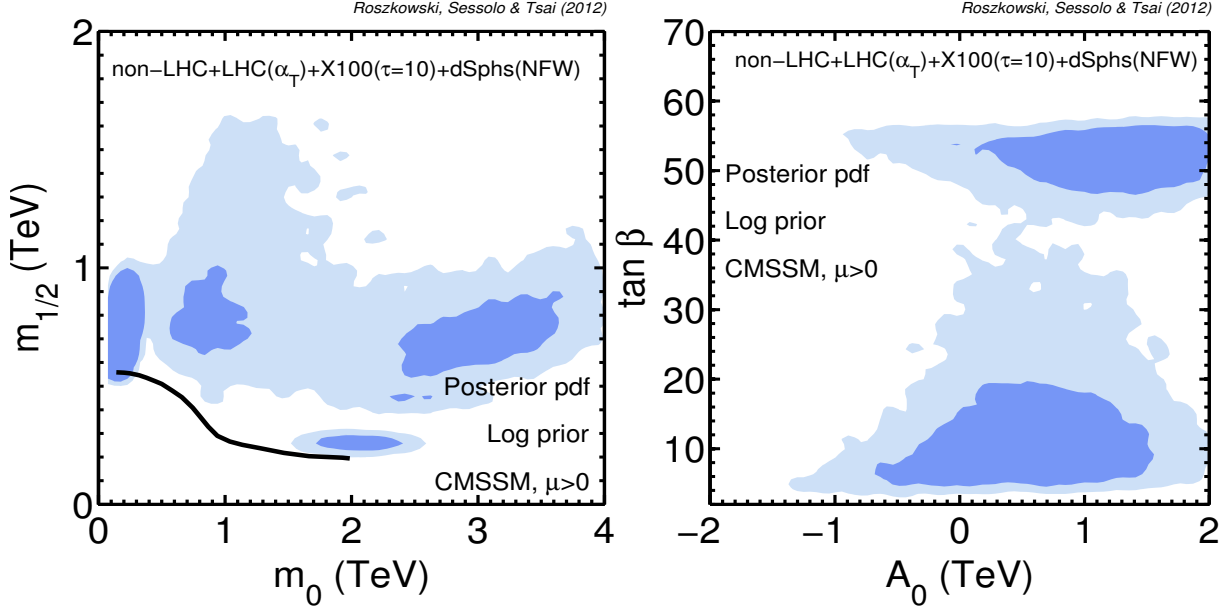


Figure 2: (a) Marginalized posterior pdf in the $(m_0, m_{1/2})$ plane. The 68% C.L. credible regions are shown in dark blue and the 95% C.L. regions in light blue. The CMSSM parameters are constrained by the non-LHC, α_T , XENON100, and dSphs data. The solid black line shows the α_T 95% C.L. exclusion bound. (b) Marginalized posterior pdf in the $(A_0, \tan \beta)$ with the same constraints as in (a).

$m_0 \sim 2500$ GeV, $m_{1/2} \sim 400$ GeV. This is because in this region the enhanced higgsino component of the neutralino produces larger $\langle \sigma v \rangle$, resulting in higher fluxes which in turn are more strongly constrained by the FermiLAT data.

One can notice in Fig. 2(a) the appearance of a new high-probability region just above the α_T limit, at $m_0 \sim 2$ TeV and $m_{1/2} \sim 300$ GeV. It is due to the Higgs-resonance mechanism through which the relic abundance constraint is satisfied, and it is not affected by the dSphs bound. Given the closeness of this island to the α_T upper bound, we investigated the possible effects on it of those LHC limits which are more sensitive to the region of PS at large m_0 [55, 56]. We applied a smeared cut at $m_{1/2} \sim 280$ GeV (which, it is worth saying, is not a procedure that has the statistical rigor of our reconstructed α_T likelihood), and we saw that the Higgs-resonance region disappeared. We conclude that this region is likely to vanish if we apply a more restrictive bound from the LHC. But we confirm that the main effects of the XENON100 and dSphs bounds on the rest of the PS is completely unchanged. In particular, the latter bound forces a shift in the high-probability areas of the FP/HB region towards higher values of $m_{1/2}$, as clearly seen by comparing Figs. 2(a) and 1(a).

The effect of the above constraints on the marginalized posterior pdf in the $(A_0, \tan \beta)$ plane is

presented in Fig. 2(b). First, we have checked that, without including the dSphs γ -ray constraint, our results agreed well with those of Ref. [9]. However, since our scan spans a wider fraction of the FP/HB region, the region around $\tan\beta \sim 30 - 40$ gains higher statistical significance than reported in that paper. When the dSphs constraint is not applied, it is contained in a 95% credible region. This behavior is due to the much enlarged 1σ credible region at large m_0 and $m_{1/2} \gtrsim 300$ GeV that can be observed in Fig. 1(a). This region does not show up in [9] at the 1σ level but only at the 2σ level, and its presence here means that the experimental constraints now favor a larger fraction of the FP/HB region, which requires intermediate values of $\tan\beta$ to satisfy the relic abundance constraint.

On the other hand, one can see in Fig. 2(a) that the dSphs γ -ray flux constraint on the scattering and annihilation cross sections reduces the high-probability part of the FP region and also pushes back the statistical significance of the region at $\tan\beta \sim 40$ to less than 95% C.L. in Fig. 2(b).

5.2 Effects on the observables

We can better understand the effect of including the FP/HB region on our scan by looking at the posterior distribution of the observables relevant for DM detection: σ_p^{SI} , $\langle\sigma v\rangle$, and the neutralino-proton SD cross section σ_p^{SD} .

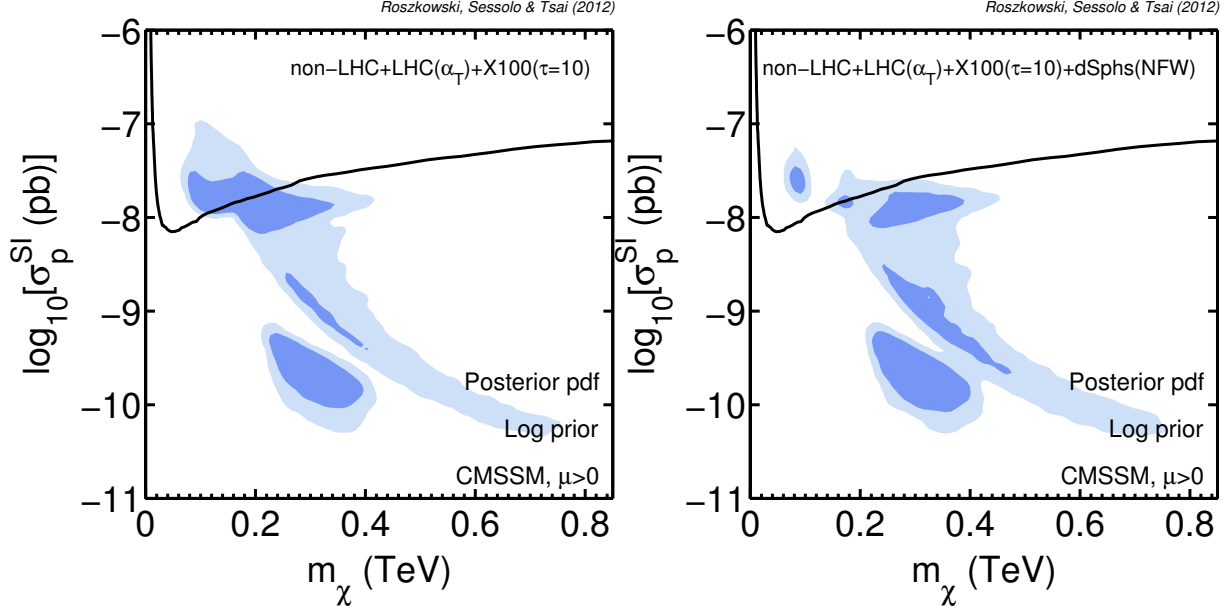


Figure 3: Marginalized posterior pdf in the $(m_\chi, \sigma_p^{\text{SI}})$ plane. The 68% C.L. credible regions are shown in dark blue and the 95% C.L. regions in light blue. (a) The impact of the non-LHC, α_T , and XENON100 constraints. (b) The impact of the non-LHC, α_T , XENON100, and dSphs constraints. The solid black line shows the XENON100 90% C.L. exclusion bound.

In Fig. 3(a) we show the posterior pdf projected on the $(m_\chi, \sigma_p^{\text{SI}})$ plane, with the non-LHC, α_T , and XENON100 (assuming $\tau = 10 \times \sigma_{p,90}^{\text{SI}}$) constraints imposed. The solid black line shows the XENON100 90% C.L. bound, although we again emphasize that we implement it with a smearing through our likelihood function and not as a hard cut. One can recognize three familiar high-probability regions. A roughly horizontal one corresponds to the FP/HB region. One (mostly 2σ credible region but with a narrow 1σ piece) decreasing with m_χ is given by the A -resonance effect. Finally, an island of high probability at $200 \text{ GeV} \lesssim m_\chi \lesssim 400 \text{ GeV}$ corresponds to the stau-coannihilation region.

A comparison with the corresponding figure in [9] shows the emergence of a sizeable 1σ credible region above the experimental bound, for lower $m_\chi \lesssim 200 \text{ GeV}$. As stated above, this is a direct consequence of our extension to include a much larger part of the FP/HB region. Figure 3(a) confirms that the XENON100 bound itself does not much affect the statistical significance of this region of PS, due to the large theoretical uncertainties associated with σ_p^{SI} .

The effect of applying the dSphs bound is shown in Fig. 3(b). One can see a significant reduction of the posterior in the nearly horizontal FP/HB region at $\sigma_p^{\text{SI}} \sim 10^{-8} \text{ pb}$. One can also see that this reduction is comparable in size to those from the XENON100 bound if the theoretical uncertainties had a much reduced size. We have indeed checked that the case X100($\tau = 1$) would not present noticeable differences with Fig. 3(b). This fact was already hinted at when comparing Figs. 1(b) and 2(a), and shows how completely different experiments can in principle be competitive in testing the CMSSM. The small high-probability island that appears in the region at large σ_p^{SI} and small m_χ of Fig. 3(b) corresponds to the Higgs-resonance region of the $(m_0, m_{1/2})$ plane, already seen in Fig. 2(a). We emphasize here that, in light of those LHC SUSY searches that are more sensitive to the large m_0 region, that island at small m_χ is likely to be excluded in future analyses. The overall reduction of the posterior in the FP/HB region, though, will be unaltered.

Figure 4 shows the marginalized posterior pdf in the $(m_\chi, \langle\sigma v\rangle)$ plane. To start with, the effect of applying only the non-LHC and α_T constraints is presented in Fig. 4(a), where one can see a familiar high-probability horizontal region at $\langle\sigma v\rangle_{\text{ann}} \sim 3 \times 10^{-26} \text{ cm}^{-3} \text{ s}^{-1}$, which arises in order to satisfy the relic abundance constraint from neutralino pair-annihilation in the FP/HB and A -resonance regions. These two different mechanisms produce comparable but slightly different $\langle\sigma v\rangle_{\text{ann}}$, a fact that reflects in the appearance of a “hole” in the posterior high-probability area. The hole is due to the conjunction of two different branches: the lower one, at $\langle\sigma v\rangle_{\text{ann}} \sim 10^{-26} \text{ cm}^{-3} \text{ s}^{-1}$, is due to annihilation in the A -funnel region of the CMSSM; the upper one, closer to $\langle\sigma v\rangle_{\text{ann}} \sim 3 \times 10^{-26} \text{ cm}^{-3} \text{ s}^{-1}$, is due to annihilation in the FP/HB (and bulk) region instead. The little vertical “tail” at $m_\chi \lesssim 100 \text{ GeV}$ is due to the Higgs-resonance region, and it would likely disappear if we considered the LHC searches most sensitive to the large m_0 region, as mentioned above.

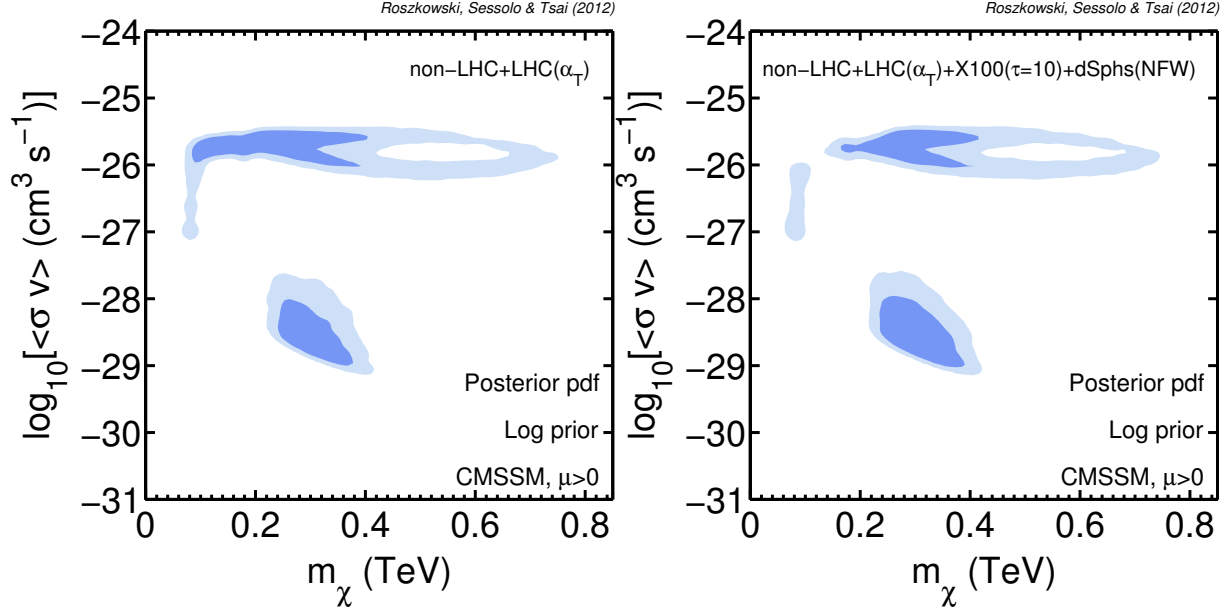


Figure 4: Marginalized posterior pdf in the $(m_\chi, \langle\sigma v\rangle_{\text{ann}})$ plane. The 68% C.L. credible regions are shown in dark blue and the 95% C.L. regions in light blue. (a) The impact of non-LHC and α_T constraints only. (b) The impact of non-LHC, α_T , XENON100, and dSphs constraints.

Additionally, there is an island of high probability at $200 \text{ GeV} \lesssim m_\chi \lesssim 400 \text{ GeV}$ and much lower $\langle\sigma v\rangle_{\text{ann}}$ corresponding to the stau-coannihilation region, where the neutralino annihilation cross section provides a subdominant contribution to the relic density.

Figure 4(b) shows the impact of dSphs when added to the non-LHC, α_T , and XENON100 constraints. It is clear that the dSphs bound disfavors the 1σ credible region at large $\langle\sigma v\rangle_{\text{ann}}$ and $100 \text{ GeV} \lesssim m_\chi \lesssim 200 \text{ GeV}$, as over there one obtains the highest γ -ray flux through the ratio $\langle\sigma v\rangle_{\text{ann}}/m_\chi^2$ in Eq. (7). On the other hand, the 1σ credible region at $m_\chi > 200 \text{ GeV}$ remains unconstrained by DD and ID experiments, even when idealized low uncertainties on DD are assumed.

5.3 Effects due to IceCube

In this subsection we analyze the effect on the CMSSM of the projected one-year 95% C.L. experimental sensitivities for the 80-string configuration at IceCube and the impact of the additional six DeepCore strings. In the assumption of equilibrium in the Sun, the event rates depend directly on the neutralino capture rate and, consequently, are most strongly dependent on the SD scattering cross section (although for some regions of PS the SI cross section can be important [53]).

In both panels of Fig. 5 we plot the marginalized pdf in the $(m_\chi, \sigma_p^{\text{SD}})$ plane, after applying all of the constraints discussed above. In Fig. 5(a) we show the case including the large uncertainties for DD searches and in Fig. 5(b) the one with reduced uncertainties. The three black lines show the

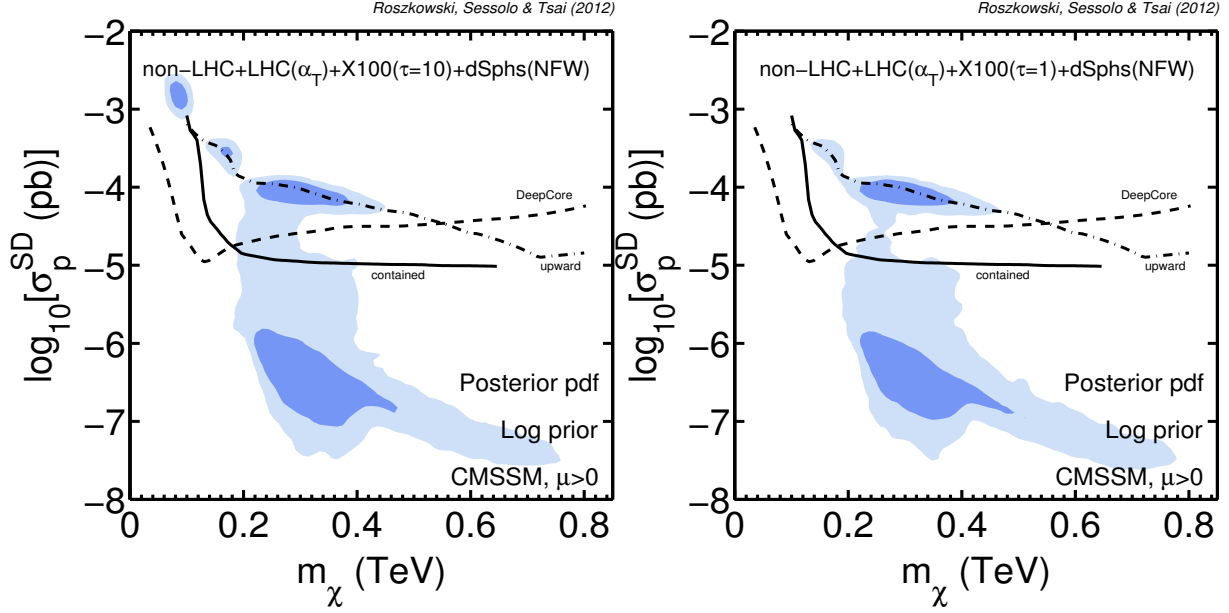


Figure 5: Marginalized posterior pdf in the $(m_\chi, \sigma_p^{\text{SD}})$ plane. The 68% C.L. credible regions are shown in dark blue and the 95% C.L. regions in light blue. (a) The impact of the non-LHC, α_T , XENON100, and dSphs constraints. (b) The impact of non-LHC, α_T , XENON100, and dSphs constraints when the theoretical uncertainty on XENON100 is reduced. The solid line is the one-year 95% C.L. sensitivity in contained events at IceCube, the dashed line the corresponding sensitivity for DeepCore, and the dash-dotted line the sensitivity in upward events.

projected sensitivities of the IceCube detection channels considered in this work. The dash-dotted line shows the sensitivity for upward events at IceCube, the solid line the sensitivity in contained events, and the dashed line the sensitivity for DeepCore. We confirm the complementarity of the three configurations to test different ranges in the neutralino mass [44, 45]. Due to its denser array, DeepCore has a lower energy threshold, so that it is better suited to probe the region at low mass, $m_\chi \sim 100$ GeV, where it could in principle compete with direct SUSY searches. As the DM mass increases, though, the neutrino flux becomes suppressed by $1/m_\chi^2$, so that the bigger volume available in the IceCube 80-string configuration becomes more important. The result is increased sensitivities in the larger detector, which can overcome the observational capabilities of DeepCore.

In the first three panels of Fig. 6, we show the posterior probability in the $(m_\chi, N_{\text{events}})$ plane, where the muon rates at the detector, $N_{\text{events}}^{\text{up}}$ [Fig. 6(a)], $N_{\text{events}}^{\text{C}}$ [Fig. 6(b)], and $N_{\text{events}}^{\text{DC}}$ [Fig. 6(c)] are given in Eqs. (11), (12), and (13), respectively. In dark blue one can see three 1σ credible regions in the mass range $200 \text{ GeV} \lesssim m_\chi \lesssim 400 \text{ GeV}$. Since they correspond to the two high-probability regions depicted in Fig. 5 for the same mass range, the splitting of the lower regions indicates some dependence on SI interactions.

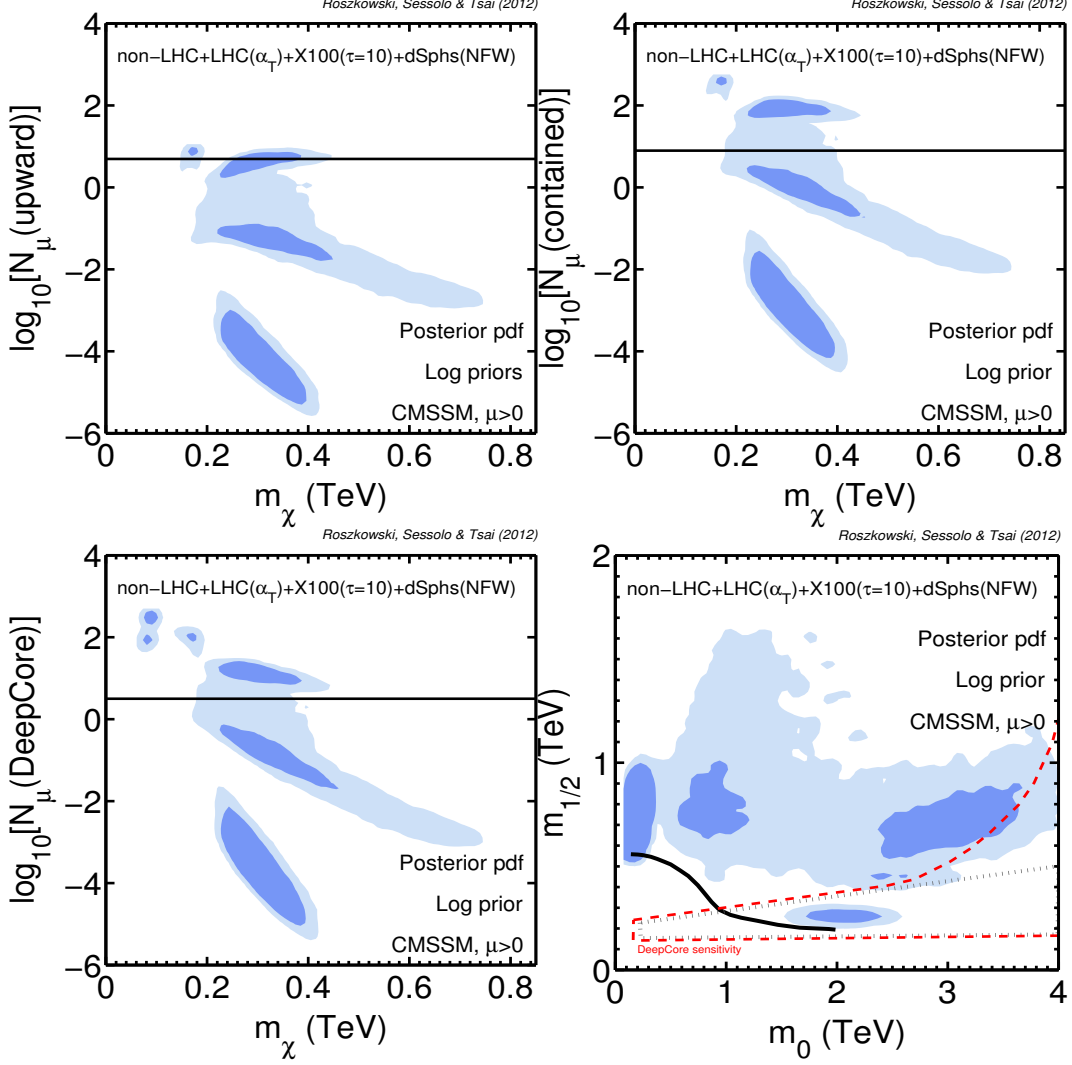


Figure 6: (a)–(c) Marginalized posterior pdf in the $(m_\chi, N_{\text{events}})$ plane. The 68% C.L. credible regions are shown in dark blue and the 95% C.L. regions in light blue. (d) Marginalized posterior pdf in the $(m_0, m_{1/2})$ plane with DeepCore one-year 95% C.L. sensitivity (inside red dashed lines, 90% of the points are above sensitivity; inside gray dotted lines, 100% of the points are above sensitivity). In all plots, the constraints are non-LHC, α_T , XENON100, and dSphs. Upward events at IceCube are shown in (a), contained events in (b), and events at DeepCore in (c).

Additionally, in the low m_χ region of Fig. 6(c) one can spot three little high-probability islands. The one at the highest mass corresponds to the little 68% credible region in the FP/HB portion of Fig. 6(d), at $m_{1/2}$ around 400 – 500 GeV. The two connected islands at an even lower mass scale, instead, correspond to the Higgs-resonance region. Their separation might be an indication of slight sampling issues, due to the fact that there are not many scan points generated close to the α_T bound.

For contained events in IceCube, and for DeepCore, about 20 – 25% of the 2σ -favored PS is above the projected sensitivity, thus indicating that the next round of data from the IceCube Collaboration has the potential to significantly constrain the PS. In Fig. 6(d) we show the region of PS in the $(m_0, m_{1/2})$ plane which is above the sensitivity at DeepCore. The region bounded by the gray (dotted) lines represents the region of parameter space for which *all* of the points in the scan are above the DeepCore sensitivity. The region bounded by the red (dashed) lines yields instead approximately 90% of the points above the DeepCore (or IceCube contained) sensitivity. One can see that it extends beyond the region tested by the FermiLAT γ -ray flux from dSphs. It appears clear that, even if the Higgs-resonance region were to be excluded by higher LHC sensitivities in the large m_0 region, the impact of DeepCore/IceCube on the FP/HB region would nonetheless be significant.

Some very enticing possibilities arise in the case that IceCube/DeepCore lives up to its expected discovery potential. In particular, we found that if the projected sensitivities are achieved, and the experimental and theoretical uncertainties are kept reasonably small, in one year DeepCore could rule out the fraction of the FP region which is mostly responsible for neutralino annihilation to W^+W^- at the 95% C.L. To illustrate this point we show in Fig. 7 the impact of some of the exclusion bounds and projected sensitivities considered in this work on models with a single predominant neutralino annihilation channel. Each point represents a case for which neutralinos annihilate 90% of the time to the selected final state, and for which the bound on the relic abundance is respected ($0.05 < \Omega_\chi h^2 < 0.20$). The likelihood used to draw the point distribution in space is subject to all of the constraints discussed above. We show in Fig. 7(a) the impact of the contained event sensitivity (black horizontal line) on these models. It is more constraining than the upward event sensitivity (not shown), but no final state can be excluded in one year of observation. On the other hand, Fig. 7(b) shows the same analysis for DeepCore. One can see that the WW channel could be excluded at the 95% C.L., and so could any CMSSM-like model for which the DM annihilates into W^+W^- . The advantage of DeepCore comes from the lower energy threshold. Since the WW channel opens up around m_W , which is very close to the threshold predicted for the IceCube's larger volume, there is not enough phase space over which the muon flux can be integrated in the contained events. Consequently, the number of hits at the detector will not be sizeable. On the other hand, since the muon energy threshold at DeepCore is $E_{\min} \sim 35$ GeV, even neutralinos that annihilate into the WW channel can provide enough muon events to be successfully detected. One can see in Fig. 7(c) that the Higgs-resonance region and part of the FP region are mostly responsible for cases with predominant DM annihilation to W^+W^- . We show in Fig. 7(d) the corresponding analysis for the XENON100 exclusion bound on σ_p^{SI} (black line). A fraction of the cases that annihilate to W^+W^- are below the bound, so nothing definitive can be said about the

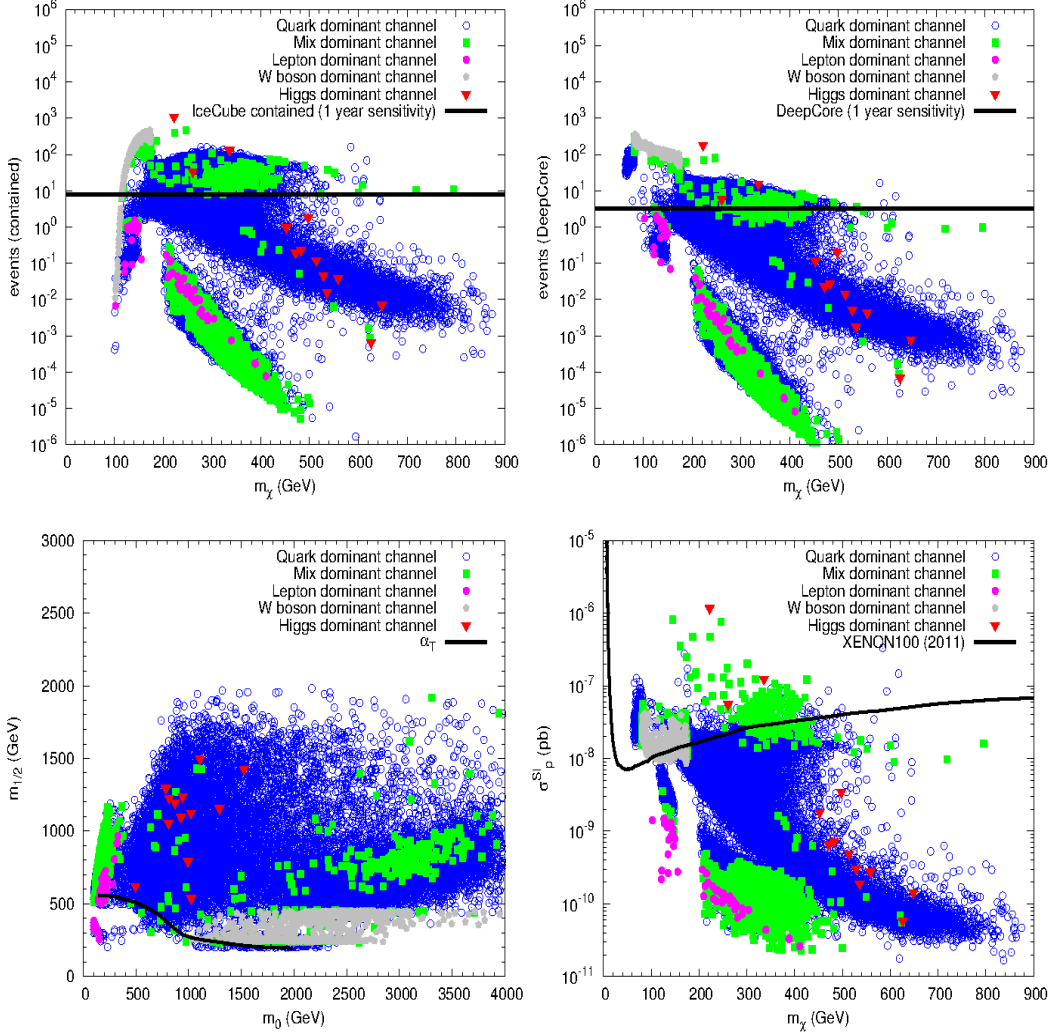


Figure 7: The impact of some of the exclusion bounds and projected sensitivities considered in this work on models with a predominant neutralino annihilation channel. (a) Projected one-year 95% C.L. sensitivity in contained events. (b) Projected sensitivity at DeepCore. (c) LHC α_T bound. (d) XENON100 bound.

exclusion potential in any channel.

6 Summary

In this paper we investigated the impact of the present bounds and projected sensitivities from DM indirect detection searches on global Bayesian inferences of the CMSSM. We applied the 95% C.L. upper bound on $\langle\sigma v\rangle$ from the recent analysis of γ -ray fluxes from dSphs by the FermiLAT Collaboration and calculated the effect of the projected one-year 95% C.L. sensitivities for neutrino

fluxes from WIMP annihilation in the Sun at IceCube and DeepCore. We also applied the constraints used in Ref. [9], with respect to which we extended our scan deep into the FP region, up to $m_0 = 4$ TeV and $m_{1/2} = 2$ TeV. In particular, we considered the recent lower bounds on sparticle masses from the CMS α_T search with 1.1 fb^{-1} integrated luminosity and the recent 90% C.L. upper bound on σ_p^{SI} from XENON100. With respect to [9], we improved the code for determination of the efficiency maps by simulating the CMS detector response with PGS4.

We found that, when the present constraints on the mass within the half-light radius are taken into account, the dSphs cross section bounds show significant constraining power on the FP/HB region. On the other hand, we confirm the findings of our previous studies that, when the theoretical uncertainties are fully taken into consideration, the constraining power of the XENON100 bound is limited. However, a less conservative (in fact, currently unrealistic) treatment of the theoretical uncertainties involved, obtained often by including only the experimental uncertainties (as given by the experimental collaboration) shows significant impact on the same region of parameter space. Even more interestingly, the DM constraints considered here, both from DD and ID, become competitive in this case. Finally, we showed that the projected one-year sensitivity at DeepCore has the potential to further constrain the FP region and to exclude the fraction of PS over which DM annihilates predominantly to W^+W^- final states. Thus, the next round of data from IceCube/DeepCore has the potential to independently rule out any new physics models whose coupling to SM particles is comparable in strength to the CMSSM and whose products of annihilation are W bosons.

Acknowledgments We would like to thank Kamila Kowalska for help during the revision of this paper. L.R. would like to thank Aldo Morselli, Eric Nuss and Alex Drlica-Wagner for useful discussions on the bounds from stellar velocity dispersions. We are funded in part by the Wellcome Programme of the Foundation for Polish Science. L.R. is also supported in part by the Polish National Science Centre Grant No. N202 167440, an STFC consortium grant of Lancaster, Manchester and Sheffield Universities and by the EC 6th Framework Program MRTN-CT-2006-035505.

References

- [1] **CMS Collaboration** Collaboration, S. Chatrchyan *et al.*, “Search for Supersymmetry at the LHC in Events with Jets and Missing Transverse Energy,” *Phys.Rev.Lett.* **107** (2011) 221804, [arXiv:1109.2352 \[hep-ex\]](#)

- [2] **ATLAS** Collaboration, G. Aad *et al.*, “Search for squarks and gluinos using final states with jets and missing transverse momentum with the ATLAS detector in $\sqrt{s} = 7$ TeV proton-proton collisions,” [arXiv:1109.6572 \[hep-ex\]](#).
- [3] H. Baer and X. Tata, “Weak scale supersymmetry: From superfields to scattering events,” Cambridge, UK: Univ. Pr. (2006).
- [4] G. L. Kane, C. F. Kolda, L. Roszkowski, and J. D. Wells, “Study of constrained minimal supersymmetry,” *Phys. Rev.* **D49** (1994) 6173–6210, [arXiv:hep-ph/9312272 \[hep-ph\]](#).
- [5] O. Buchmueller *et al.*, “Implications of Initial LHC Searches for Supersymmetry,” *Eur. Phys. J.* **C71** (2011) 1634, [arXiv:1102.4585 \[hep-ph\]](#). ; O. Buchmueller *et al.*, “Supersymmetry and Dark Matter in Light of LHC 2010 and Xenon100 Data,” *Eur. Phys. J.* **C71** (2011) 1722, [arXiv:1106.2529 \[hep-ph\]](#). ; B. Allanach, “Impact of CMS Multi-jets and Missing Energy Search on CMSSM Fits,” *Phys. Rev.* **D83** (2011) 095019, [arXiv:1102.3149 \[hep-ph\]](#). ; B. Allanach, T. Khoo, C. Lester, and S. Williams, “The impact of the ATLAS zero-lepton, jets and missing momentum search on a CMSSM fit,” *JHEP* **1106** (2011) 035, [arXiv:1103.0969 \[hep-ph\]](#). ; M. Farina *et al.*, “Implications of XENON100 and LHC results for Dark Matter models,” *Nucl. Phys.* **B853** (2011) 607–624, [arXiv:1104.3572 \[hep-ph\]](#).
- [6] O. Buchmueller *et al.*, “Supersymmetry in Light of 1/fb of LHC Data,” *Eur.Phys.J.* **C72** (2012) 1878, [arXiv:1110.3568 \[hep-ph\]](#).
- [7] S. Akula, D. Feldman, Z. Liu, P. Nath, and G. Peim, “New Constraints on Dark Matter from CMS and ATLAS Data,” *Mod. Phys. Lett.* **A26** (2011) 1521–1535, [arXiv:1103.5061 \[hep-ph\]](#).
- [8] G. Bertone *et al.*, “Global fits of the cMSSM including the first LHC and XENON100 data,” [arXiv:1107.1715 \[hep-ph\]](#). ; C. Strege *et al.*, “Updated global fits of the cMSSM including the latest LHC SUSY and Higgs searches and XENON100 data,” *JCAP* **1203** (2012) 030, [arXiv:1112.4192 \[hep-ph\]](#).
- [9] A. Fowlie *et al.*, “Bayesian Implications of Current LHC and XENON100 Search Limits for the Constrained MSSM,” *Phys.Rev.* **D85** (2012) 075012, [arXiv:1111.6098 \[hep-ph\]](#).
- [10] **XENON100** Collaboration, E. Aprile *et al.*, “The XENON100 Dark Matter Experiment,” [arXiv:1107.2155 \[astro-ph.IM\]](#).
- [11] **XENON100** Collaboration, E. Aprile *et al.*, “Likelihood Approach to the First Dark Matter Results from XENON100,” *Phys. Rev.* **D84** (2011) 052003, [arXiv:1103.0303 \[hep-ex\]](#).

- [12] **XENON100** Collaboration, E. Aprile *et al.*, “Dark Matter Results from 100 Live Days of XENON100 Data,” *Phys. Rev. Lett.* **107** (2011) 131302, [arXiv:1104.2549 \[astro-ph.CO\]](#).
- [13] J. L. Feng, K. T. Matchev, and T. Moroi, “Focus points and naturalness in supersymmetry,” *Phys. Rev.* **D61** (2000) 075005, [arXiv:hep-ph/9909334](#). ; J. L. Feng, K. T. Matchev, and F. Wilczek, “Neutralino Dark Matter in Focus Point Supersymmetry,” *Phys. Lett.* **B482** (2000) 388–399, [arXiv:hep-ph/0004043](#). ; K. L. Chan, U. Chattopadhyay, and P. Nath, “Naturalness, weak scale supersymmetry and the prospect for the observation of supersymmetry at the Tevatron and at the LHC,” *Phys. Rev.* **D58** (1998) 096004, [arXiv:hep-ph/9710473](#).
- [14] **Fermi-LAT** Collaboration, M. Ackermann *et al.*, “Constraining Dark Matter Models from a Combined Analysis of Milky Way Satellites with the Fermi Large Area Telescope,” *Phys. Rev. Lett.* **107** (2011) 241302, [arXiv:1108.3546 \[astro-ph.HE\]](#).
- [15] **IceCube** Collaboration, “IceCube - Astrophysics and Astroparticle Physics at the South Pole,” [arXiv:1111.5188 \[astro-ph.HE\]](#).
- [16] R. R. de Austri, R. Trotta, and L. Roszkowski, “A Markov chain Monte Carlo analysis of the CMSSM,” *JHEP* **0605** (2006) 002, [arXiv:hep-ph/0602028 \[hep-ph\]](#).
- [17] R. Trotta, F. Feroz, M. P. Hobson, L. Roszkowski, and R. Ruiz de Austri, “The Impact of priors and observables on parameter inferences in the Constrained MSSM,” *JHEP* **0812** (2008) 024, [arXiv:0809.3792 \[hep-ph\]](#).
- [18] <http://www.ft.uam.es/personal/rruiz/superbayes/index.php?page=main.html>
- [19] **WMAP** Collaboration, E. Komatsu *et al.*, “Seven-Year Wilkinson Microwave Anisotropy Probe (WMAP) Observations: Cosmological Interpretation,” *Astrophys. J. Suppl.* **192** (2011) 18, [arXiv:1001.4538 \[astro-ph.CO\]](#)
- [20] **Particle Data Group** Collaboration, K. Nakamura *et al.*, “Review of particle physics,” *J. Phys. G* **G37** (2010) 075021
- [21] J. P. Miller, E. de Rafael, and B. L. Roberts, “Muon (g-2): Experiment and theory,” *Rept.Prog.Phys.* **70** (2007) 795, [arXiv:hep-ph/0703049 \[hep-ph\]](#).
- [22] **Heavy Flavor Averaging Group** Collaboration, D. Asner *et al.*, “Averages of b-hadron, c-hadron, and τ -lepton Properties,” [arXiv:1010.1589 \[hep-ex\]](#)
- [23] **LHCb** Collaboration, J. Serrano, “Searches for the very rare decays $B_s/d \rightarrow \mu^+ \mu^-$ at LHCb,” EPS-HEP. Grenoble, 2011

- [24] **LEP Working Group for Higgs boson searches, ALEPH Collaboration, DELPHI Collaboration, L3 Collaboration, OPAL Collaboration**, R. Barate *et al.*, “Search for the standard model Higgs boson at LEP,” *Phys. Lett.* **B565** (2003) 61–75, arXiv:hep-ex/0306033 [hep-ex]
- [25] **ALEPH Collaboration**, A. Heister *et al.*, “Absolute mass lower limit for the lightest neutralino of the MSSM from $e^+ e^-$ data at $s^{*(1/2)}$ up to 209-GeV,” *Phys. Lett.* **B583** (2004) 247–263
- [26] **ALEPH Collaboration**, A. Heister *et al.*, “Search for scalar leptons in $e^+ e^-$ collisions at center-of-mass energies up to 209-GeV,” *Phys. Lett.* **B526** (2002) 206–220, arXiv:hep-ex/0112011 [hep-ex].
- [27] **L3 Collaboration**, P. Achard *et al.*, “Search for scalar leptons and scalar quarks at LEP,” *Phys.Lett.* **B580** (2004) 37–49, arXiv:hep-ex/0310007 [hep-ex].
- [28] LEP SUSY Working Group for the ALEPH, DELPHI, L3 and OPAL collaborations. <http://lepsusy.web.cern.ch/lepsusy>
- [29] **DELPHI Collaboration**, J. Abdallah *et al.*, “Searches for supersymmetric particles in $e^+ e^-$ collisions up to 208-GeV and interpretation of the results within the MSSM,” *Eur. Phys. J.* **C31** (2003) 421–479, arXiv:hep-ex/0311019 [hep-ex]
- [30] <http://physics.ucdavis.edu/~conway/research/software/pgs/pgs4-general.htm>
- [31] A. M. Green, “Dependence of direct detection signals on the WIMP velocity distribution,” *JCAP* **1010** (2010) 034, arXiv:1009.0916 [astro-ph.CO].
- [32] M. Pato *et al.*, “Complementarity of Dark Matter Direct Detection Targets,” *Phys. Rev.* **D83** (2011) 083505, arXiv:44903458 [astro-ph.CO].
- [33] C. Arina, J. Hamann, and Y. Y. Wong, “A Bayesian view of the current status of dark matter direct searches,” *JCAP* **1109** (2011) 022, arXiv:1105.5121 [hep-ph].
- [34] J. R. Ellis, K. A. Olive, and C. Savage, “Hadronic Uncertainties in the Elastic Scattering of Supersymmetric Dark Matter,” *Phys. Rev.* **D77** (2008) 065026, arXiv:0801.3656 [hep-ph].
- [35] **Fermi-LAT Collaboration**, W. Atwood *et al.*, “The Large Area Telescope on the Fermi Gamma-ray Space Telescope Mission,” *Astrophys. J.* **697** (2009) 1071–1102, arXiv:0902.1089 [astro-ph.IM].
- [36] A. Abdo *et al.*, “Fermi LAT Search for Photon Lines from 30 to 200 GeV and Dark Matter Implications,” *Phys. Rev. Lett.* **104** (2010) 091302, arXiv:1001.4836 [astro-ph.HE].

- [37] A. Abdo *et al.*, “Observations of Milky Way Dwarf Spheroidal galaxies with the Fermi-LAT detector and constraints on Dark Matter models,” *Astrophys. J.* **712** (2010) 147–158, [arXiv:1001.4531 \[astro-ph.CO\]](#).
- [38] P. Scott *et al.*, “Direct Constraints on Minimal Supersymmetry from Fermi-LAT Observations of the Dwarf Galaxy Segue 1,” *JCAP* **1001** (2010) 031, [arXiv:0909.3300 \[astro-ph.CO\]](#).
- [39] J. F. Navarro, C. S. Frenk, and S. D. White, “The Structure of cold dark matter halos,” *Astrophys. J.* **462** (1996) 563–575, [arXiv:astro-ph/9508025 \[astro-ph\]](#).
- [40] L. Roszkowski, R. R. de Austri, J. Silk, and R. Trotta, “On prospects for dark matter indirect detection in the Constrained MSSM,” *Phys. Lett.* **B671** (2009) 10–14, [arXiv:0707.0622 \[astro-ph\]](#).
- [41] A. Charbonnier *et al.*, “Dark matter profiles and annihilation in dwarf spheroidal galaxies: perspectives for present and future gamma-ray observatories - I. The classical dSphs,” *Mon. Not. Roy. Astron. Soc.* **418** (2011) 1526–1556, [arXiv:1104.0412 \[astro-ph.HE\]](#).
- [42] **IceCube** Collaboration, T. K. Gaisser, “IceCube: Status and Results,” [arXiv:1108.1838 \[astro-ph.HE\]](#).
- [43] M. Gonzalez-Garcia, F. Halzen, and S. Mohapatra, “Identifying Galactic PeVatrons with Neutrinos,” *Astropart. Phys.* **31** (2009) 437–444, [arXiv:0902.1176 \[astro-ph.HE\]](#).
- [44] V. Barger, J. Kumar, D. Marfatia, and E. M. Sessolo, “Fermion WIMPless Dark Matter at DeepCore and IceCube,” *Phys. Rev.* **D81** (2010) 115010, [arXiv:1004.4573 \[hep-ph\]](#).
- [45] V. Barger, Y. Gao, and D. Marfatia, “Dark matter at DeepCore and IceCube,” *Phys. Rev.* **D83** (2011) 055012, [arXiv:1101.4410 \[hep-ph\]](#).
- [46] **IceCube** Collaboration, R. Abbasi *et al.*, “Limits on a muon flux from neutralino annihilations in the Sun with the IceCube 22-string detector,” *Phys. Rev. Lett.* **102** (2009) 201302, [arXiv:0902.2460 \[astro-ph.CO\]](#).
- [47] **IceCube** Collaboration, “Multi-year search for dark matter annihilations in the Sun with the AMANDA-II and IceCube detectors,” [arXiv:1112.1840 \[astro-ph.HE\]](#).
- [48] R. Trotta, R. Ruiz de Austri, and C. Perez de los Heros, “Prospects for dark matter detection with IceCube in the context of the CMSSM,” *JCAP* **0908** (2009) 034, [arXiv:0906.0366 \[astro-ph.HE\]](#). ; G. Bertone, D. Cumberbatch, R. R. de Austri, and R. Trotta, “Dark Matter Searches: The Nightmare Scenario,” [arXiv:1107.5813 \[astro-ph.HE\]](#).

- [49] S. Profumo, “The Quest for Supersymmetry: Early LHC Results versus Direct and Indirect Neutralino Dark Matter Searches,” *Phys. Rev.* **D84** (2011) 015008, [arXiv:1105.5162 \[hep-ph\]](#).
- [50] R. Allahverdi, S. Bornhauser, B. Dutta, and K. Richardson-McDaniel, “Prospects for Indirect Detection of Sneutrino Dark Matter with IceCube,” *Phys. Rev.* **D80** (2009) 055026, [arXiv:0907.1486 \[hep-ph\]](#). ; R. Allahverdi and K. Richardson, “Distinguishing among dark matter annihilation channels with neutrino telescopes,” [arXiv:1201.6603 \[hep-ph\]](#).
- [51] A. E. Erkoca, M. H. Reno, and I. Sarcevic, “Muon Fluxes From Dark Matter Annihilation,” *Phys. Rev.* **D80** (2009) 043514, [arXiv:0906.4364 \[hep-ph\]](#).
- [52] P. Lipari and T. Stanev, “Propagation of multi - TeV muons,” *Phys. Rev.* **D44** (1991) 3543–3554.
- [53] P. Gondolo *et al.*, “DarkSUSY: Computing supersymmetric dark matter properties numerically,” *JCAP* **0407** (2004) 008, [arXiv:astro-ph/0406204 \[astro-ph\]](#).
- [54] M. Blennow, J. Edsjo, and T. Ohlsson, “Neutrinos from WIMP annihilations using a full three-flavor Monte Carlo,” *JCAP* **0801** (2008) 021, [arXiv:0709.3898 \[hep-ph\]](#).
- [55] “Search for supersymmetry with the razor variables at CMS,” Tech. Rep. CMS-PAS-SUS-11-008, CERN, Geneva, 2011
- [56] “Search for supersymmetry in all-hadronic events with missing energy,” Tech. Rep. CMS-PAS-SUS-11-004, CERN, Geneva, 2011